SI Appendix

Results and Discussion

Measurement of $^{86}Rb^+$-binding to H^+,K^+-ATPase. Because fluorinated phosphate analogues, such as aluminum fluoride (AlF), beryllium fluoride (BeF), and magnesium fluoride (MgF), mimic the chemical structure of phosphate, these compounds have been used for structural analyses of several P-type ATPase isoforms. We previously characterized the effects of these complexes on H^+,K^+-ATPase, and found that adding high concentrations of Mg^{2+} to the AlF-inhibited enzyme induced the dissociation of AlF, which resulted in recovery of the ATPase activity. This Mg^{2+}-induced reactivation is strongly suppressed (*i.e.*, ATPase activity remains inhibited) by millimolar amounts of K^+ (1). To directly confirm K^+-binding to the AlF-inhibited H^+,K^+-ATPase, we determined the amount of bound $^{86}Rb^+$, a K^+ congener that has similar effects on either ATPase activity or the suppression of Mg^{2+}-induced reactivation (Figs. S2, S3).

The $^{86}Rb^+$-concentration dependence of the amount of $^{86}Rb^+$ incorporated into the membrane preparation of H^+,K^+-ATPase in the presence or absence of AlF is shown in Fig. S4*A*. The amount of $^{86}Rb^+$ that was specifically bound to the AlF-inhibited H^+,K^+-ATPase was calculated as the difference between that in the presence and absence of AlF, because the linearly increasing concentration-dependent component was likely to be responsible for the non-specifically incorporated $^{86}Rb^+$ into the residual trapped space, such as the remaining tight and/or multilamellar vesicles within the SDS-treated H^+,K^+-ATPase preparations. This notion is also supported by the relatively slow incorporation of the total amount of $^{86}Rb^+$ ($\tau_{0.5(-AlF)}$ = 3 min, $\tau_{0.5(+AlF)}$ =

1.5 min) into the sample, which is unlikely to be a catalytic reaction by the H^+,K^+-ATPase enzyme, in contrast to the rapid increase ($\tau_{0.5}$ < 0.3 min) in the amount of AlF-dependent $^{86}Rb^+$-binding (Fig. S4*B*). Although the determined stoichiometry was around 0.15 mole of bound Rb^+ per molecule (0.3 nmol $^{86}Rb^+$/mg *versus* 2 nmol ^{32}P phosphoenzyme/mg), the data qualitatively suggest that Rb^+ is bound to the AlF-inhibited H^+,K^+-ATPase with high affinity ($K_{0.5}$ = 16 μM, Fig. 1*B*), compared with VO_4-inhibited H^+,K^+-ATPase ($K_{0.5}$ = 0.29 mM, the value from ref. 2) or overall H^+,K^+-ATPase activity ($K_{0.5}$ = 0.9 mM, Fig. 3*A*).

We also compared the effect of various inhibitors on the amount of bound Rb^+. As shown in the inset of Fig. 1*B*, the amount of bound $^{86}Rb^+$ was highest for the AlF-inhibited enzyme, in contrast to inhibition by BeF or SCH28080 (a K^+-competitive acid blocker, ref. 3), both of which induced $^{86}Rb^+$-binding comparable to the background value. $^{86}Rb^+$-binding to the MgF-inhibited enzyme is likely because Mg^{2+}-induced reactivation of MgF-inhibited enzyme is also suppressed by K^+, as shown previously (1), although the magnitude is much smaller than in the case of AlF. The low level of $^{86}Rb^+$-binding to the VO_4-inhibited enzyme was caused by low-affinity Rb^+-binding to the VO_4-inhibited enzyme, because the concentration of $^{86}Rb^+$ for this measurement is 0.5 mM.

In Na^+,K^+-ATPase, occluded Rb^+ should be in equilibrium with bound (but not occluded) Rb^+, and the maximal amount of occluded Rb^+ will be equal to the number of transport sites only if the equilibrium between these two states is strongly poised toward the occluded state (4). This condition should also apply for Rb^+ bound to the AlF-H^+,K^+-ATPase complex. The failure to measure stoichiometric $^{86}Rb^+$ incorporation into H^+,K^+-ATPase is therefore due to insufficient stabilization by AlF to

accumulate all H^+,K^+-ATPase molecules in the $^{86}Rb^+$-occlusion state, *i.e.*, H^+,K^+-ATPase molecule that occlude $^{86}Rb^+$ should be in equilibrium with bound $^{86}Rb^+$, the latter of which is exchangeable during washing with an excess amount of cold Rb^+.

As described above, Mg^{2+}-induced reactivation is suppressed in the presence of millimolar concentrations of Rb^+ (Fig. S3*B*). If Rb^+ is stably occluded by the AlF-inhibited enzyme, then Mg^{2+}-induced reactivation should remain suppressed even when Rb^+ is diluted below its effective concentration for the suppression. Regardless of pre-incubation with Rb^+, however, the suppression effect was not observed (*i.e.*, restoration of ATPase activity) in the absence of Rb^+, in contrast to the strong suppression in the presence of Rb^+ (Fig. S2). Therefore, as expected by the low-level of $^{86}Rb^+$-binding, these data indicate the Rb^+ bound to the AlF-inhibited enzyme is not stably occluded, but is exchangeable and can dissociate when diluted, at least under the conditions examined here. Conversely, regardless of whether Rb^+ was bound or occluded, the AlF-inhibited enzyme distinctly strongly suppressed Mg^{2+}-reactivation in the presence of sufficiently high concentrations of Rb^+ (Fig. 1*A*); thus, the enzyme must accumulate in a conformational state different from *E2*AlF with high occupancy of bound Rb^+ in its cation-binding site.

Measurement of $^{86}Rb^+$-binding to the Mg^{2+}-reactivated enzyme showed an inverse relationship between its ATPase activity and the amount of bound $^{86}Rb^+$ (Fig. S5*A*). The apparent affinity of Rb^+ for the suppression ($K_{0.5}$ = 53 μM) was close to that for the amount of bound $^{86}Rb^+$ ($K_{0.5}$ = 68 μM) under the same experimental conditions (*i.e.*, in the presence of 10 mM Mg^{2+}), and distinguishable from that for $^{86}Rb^+$ binding in the absence of Mg^{2+} ($K_{0.5}$ = 16 μM) in our measurements (Fig. S5*B*). These data suggest that the observed suppression effect of Rb^+ was due to its direct binding to the

AlF-inhibited enzyme. Thus, although it is somewhat qualitative, we conclude that our $^{86}Rb^+$ measurement reflects the Rb^+-binding property of H^+,K^+-ATPase.

Two-dimensional crystallization of H^+,K^+-ATPase with fluorinated phosphate analogues and Rb^+ or K^+. To our surprise, the addition of Rb^+ to the AlF-containing solution produced large and well-ordered 2D crystals (Fig. S6) compared with its absence, which might reflect the stabilizing properties of Rb^+ on Mg^{2+}-induced reactivation, as described above. Such a large morphology change was also observed for 2D crystals with AlF and K^+. Because the crystals broke when they were washed with Rb^+- or K^+-free buffer, H^+,K^+-ATPase molecules in these 2D crystals were expected to assume a conformation different from that under Rb^+-free conditions. On the other hand, consistent with our $^{86}Rb^+$ measurement, the addition of Rb^+ to the BeF crystals affected neither their morphology nor crystal quality (Fig. S6*D*, *E*), suggesting that the conformation of the BeF-bound form of H^+,K^+-ATPase is unlikely to be affected by Rb^+. Although the suppression effect of K^+ is also observed for the MgF-inhibited enzyme (1), we did not perform crystallization trials with MgF and Rb^+or K^+, because no crystalline array was formed in the presence of MgF alone (Fig. S6*F*) probably due to the limited inhibitory effect of MgF.

Rb^+-induced conformational changes at the cytoplasmic domains. Like other medium-resolution structures of H^+,K^+-ATPase, EM maps of Rb^+-bound (Rb^+)*E2*~AlF (Fig. 2*A*) and K^+-bound form (K^+)*E2*~AlF (Fig. S12) show expected features such as separate cylindrical densities for α helices and recognizable envelopes of each domain. In contrast to the density at the cation-binding site described in the

main text, these two structures showed no detectable conformational difference, including in the N-terminal tail of the β-subunit (Fig. S12). On the other hand, comparison of the cytoplasmic domains between Rb^+-free *E2*AlF (ref. 5) and (Rb^+)*E2*~AlF revealed important differences (Fig. S7). Notably, the density responsible for the bound ADP at the N domain of Rb^+-free *E2*AlF was absent in the (Rb^+)*E2*~AlF, despite its abundance (1 mM) in the crystallization solution (Fig. 3). This Rb^+-induced dissociation of ADP was related to subtle changes in the relative orientations of the cytoplasmic domains, which were located more than 30Å away from the cation-binding site in the membrane (Fig. S7*C*, Movie S2). Movement of the A domain away from the N domain may decrease ADP affinity, because the diphosphate portion of ADP seems to interact with the outermost part of the A domain, similar to the regulatory mode of nucleotide binding observed in the SERCA (TG)*E2*·MgF·ADP structure (6).

Implications for the conformational changes observed at the cytoplasmic domains. Dephosphorylation of *E2*P is largely accelerated by binding of the counter-transported cations. In the case of SERCA, the presence of AlF alone induces an *E2*~P transition state analogue due to the abundance of counter-transported H^+ ions. This is not the case for H^+,K^+-ATPase, however, because, in addition to AlF, the gastric enzyme requires K^+ (or Rb^+) as a counter-ion to form a transition state of dephosphorylation. Interestingly, K^+-free *E2*AlF and *E2*BeF generate an almost identical luminal-closed conformation in our EM maps (1, 5), in contrast to the significant conformational difference between X-ray structures of SERCA in the luminal-open *E2*BeF ground state and the luminal-closed *E2*~AlF transition state (7).

We thus concluded that such a luminal-closed conformation of *E2*P might be energetically favorable for H^+,K^+-ATPase to prevent proton reverse-flow from the luminal face of the enzyme (1). In the present study, addition of the counter-ion Rb^+ or K^+ to the *E2*AlF reveals not only its direct binding to the cation-binding site, but also an allosteric effect on the overall conformation, the latter of which resulted in the dissociation of the βNt from the P domain (Fig. 3), and of the ADP molecule from the N domain (Fig. S7). Interestingly, movement of the A domain away from the P domain led us to suggest a different coordination geometry of the TGES-motif with BeF or AlF at the phosphorylation site of the X-ray structures of SERCA (8). Therefore, we conclude that the present (Rb^+)*E2*~AlF structure most likely represents the "canonical" *E2*~P transition state, which is distinct from the preceding Rb^+-free *E2*P state.

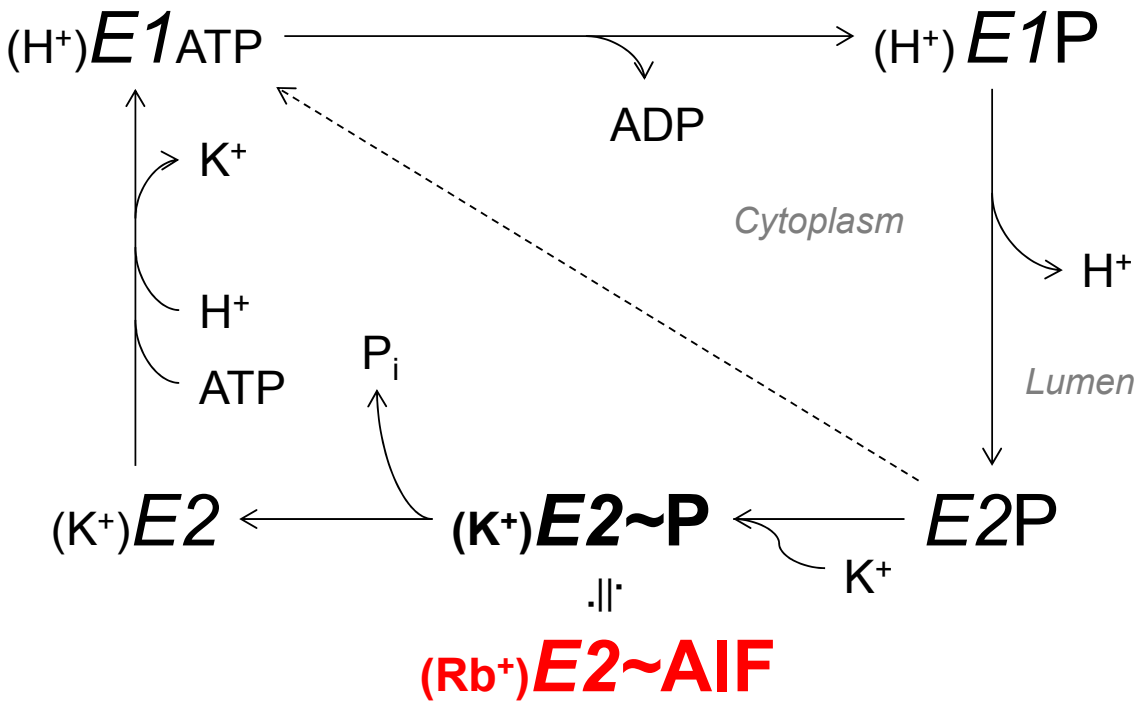

Fig. S1. *Reaction scheme of H^+,K^+-ATPase.* Ion transport and ATP hydrolysis are coupled to the cyclic conformational conversions of the enzyme. Proton binding to the cytoplasmic-open *E1* conformation activates autophosphorylation (9) from the Mg^{2+}-ATP to form *E1*P, which is soon converted to *E2*P by transporting H^+ against its steep gradient. Binding of luminal K^+, or its congener Rb^+, to the *E2*P conformation stimulates dephosphorylation, and then drives the enzyme into a (K^+)*E2* conformation. Subsequently, the conformational change to *E1* form occurs and the K^+ ions are released to the cytoplasm. In the absence of K^+, however, the spontaneous dephosphorylation of *E2*P is the rate-limiting step, thus ATPase activity (Fig. S3) and proton transport (29) is almost negligible. Therefore, acceleration of *E2*P dephosphorylation by the binding of counter-transported K^+ is prerequisite for the maximum turnover of the H^+,K^+-ATPase. Although each reaction step is reversible, only the forward direction is indicated by the arrows. The dotted arrow indicates spontaneous slow dephosphorylation of *E2*P in the absence of K^+. As described in the text, the present (Rb^+)*E2*~AlF structure would be a structural analogue of the transition state of the K^+-induced *E2*P-dephosphorylation (indicated in red).

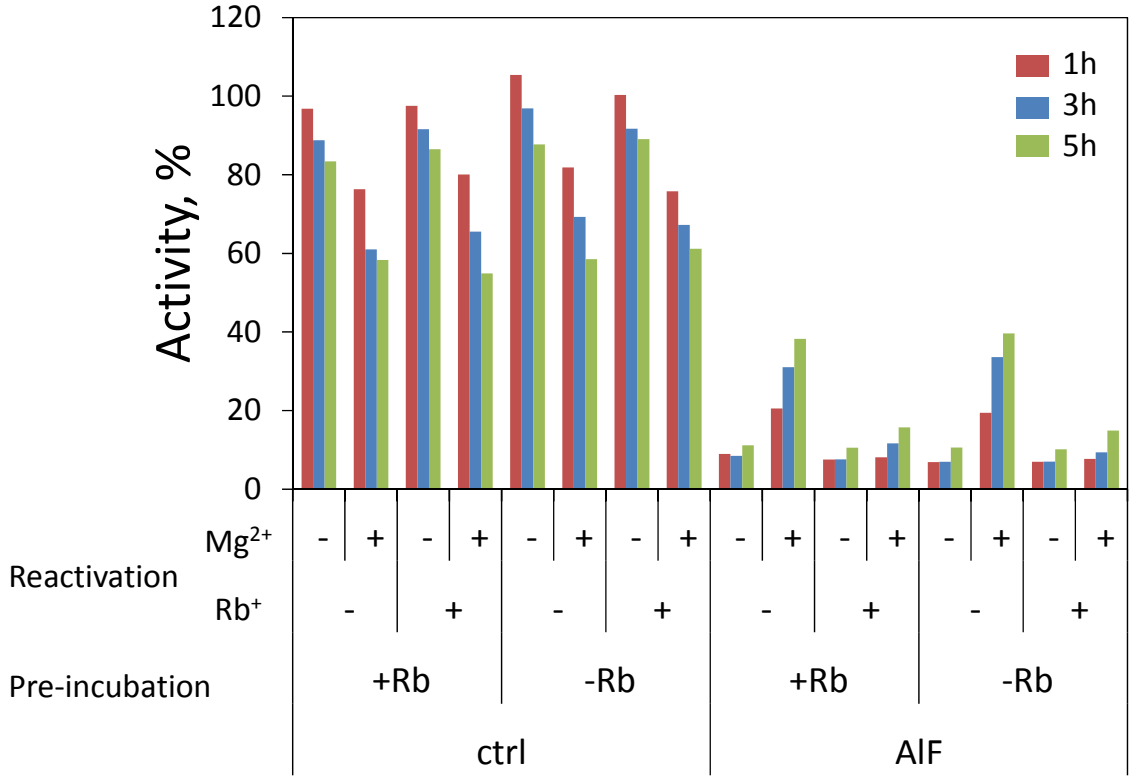

Fig. S2. *Effect of Rb^+-preincubation on its suppression effect for the Mg^{2+}-induced reactivation of the AlF-inhibited H^+,K^+-ATPase.* Control (ctrl) or AlF-inhibited (AlF) enzyme preparations were pre-incubated with (+Rb) or without (-Rb) 1 mM Rb^+ for 1 h (Pre-incubation). Samples were then diluted 1000-fold (thus, Rb^+ carried over from each sample is diluted below its required concentration for suppression) with or without 10 mM Mg^{2+} and/or 1 mM Rb^+, as indicated in the figure, (Reactivation) for 1, 3, or 5 h (red, blue or green bars, respectively) at 37°C. The ATPase activities of these samples were then determined. The mean value of the specific ATPase activity of the control samples at 1h was defined as 100%.

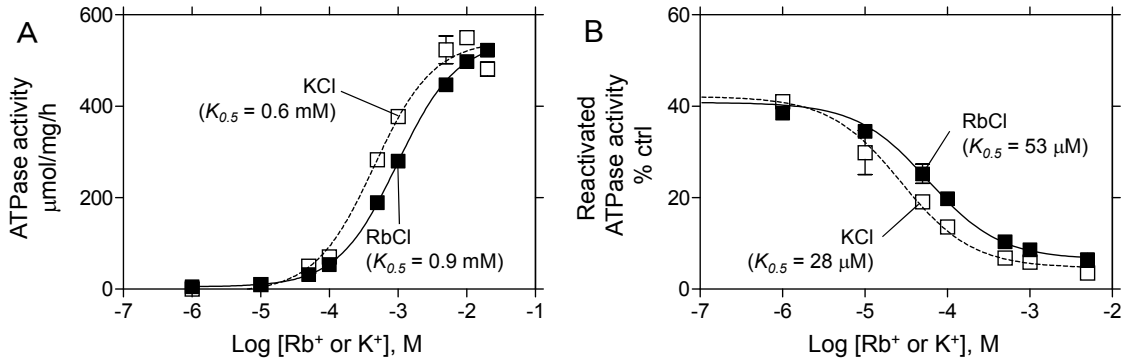

Fig. S3. *Effect of K^+ and Rb^+ on the ATPase activity, and the suppression effect for the Mg^{2+}-induced reactivation.* (*A*) Rb^+- (closed squares) or K^+-dependent (open squares) ATPase activities in the SDS-purified membrane fractions from pig stomach. ATPase activity in the presence of 0.1 mM SCH28080 is set as a blank. (*B*) Suppression effect of the indicated concentrations of Rb^+ or K^+ on the Mg^{2+}-induced reactivation (37°C for 5h) of the AlF-inhibited enzyme. Values are plotted as percentage of the ATPase activity in the control sample, as in Fig. 1*A*.

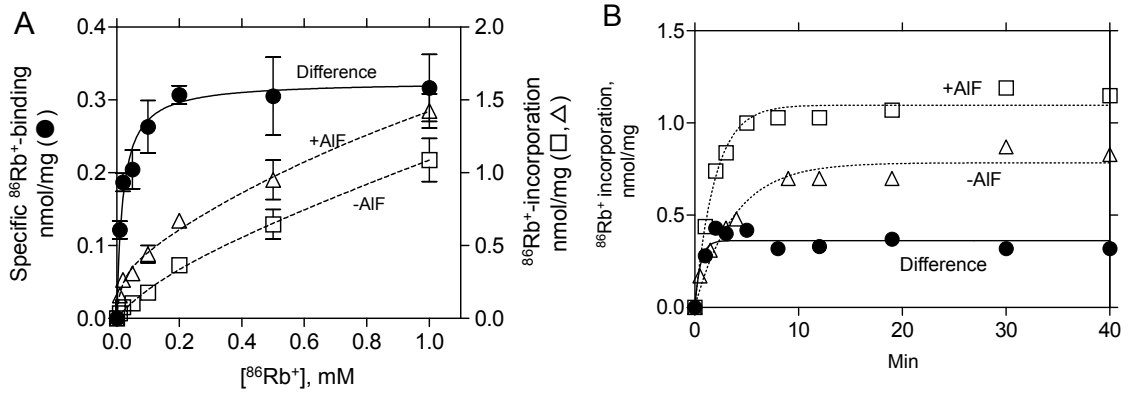

Fig. S4. *Measurement of $^{86}Rb^+$-binding to the H^+,K^+-ATPase.* (*A*) Rb^+-concentration dependence of the amount of bound $^{86}Rb^+$. Membrane preparations of H^+,K^+-ATPase treated with (open triangles) or without (open squares) AlF, were incubated in the presence of the indicated concentrations of $^{86}Rb^+$ for 30 min at 37°C. The total amount of incorporated $^{86}Rb^+$ was determined (plotted according to the right axis). The amount of $^{86}Rb^+$ specifically bound to the H^+,K^+-ATPase (closed circles) was then calculated as the difference between +AlF and –AlF samples (left axis). (*B*) Time course of $^{86}Rb^+$-binding. Samples with or without AlF-inhibition were incubated for the indicated times at 37°C in the presence of 0.5 mM $^{86}Rb^+$. Symbols were used as in (*A*).

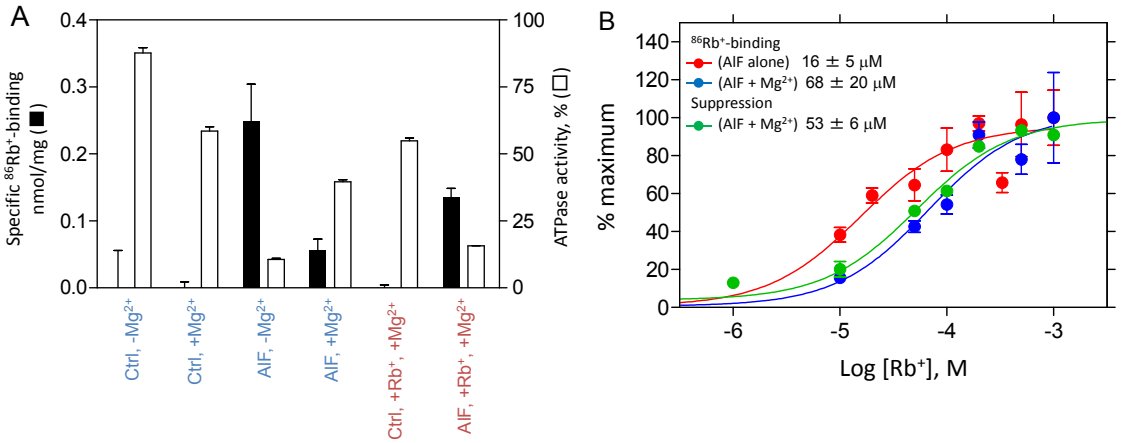

Fig. S5. *Relationship between $^{86}Rb^+$-binding and Mg^{2+}-induced reactivation.* (*A*) Comparison of the amount of $^{86}Rb^+$-binding and residual ATPase activities. Control (Ctrl) or AlF-inhibited enzyme (AlF) preparations were incubated in the presence or absence of Mg^{2+} ($\pm Mg^{2+}$) for 4.5 h at 37°C, followed by additional incubation with 0.5 mM $^{86}Rb^+$ for 30 min. For Rb^+-suppression samples ($+Rb^+$), enzymes were incubated in the presence of Mg^{2+} and $^{86}Rb^+$ for 5 h at 37°C. The amount of $^{86}Rb^+$-binding (closed columns) and ATPase activity (open columns) in each sample was measured. (*B*) Concentration dependence on Rb^+ of the amount of $^{86}Rb^+$-binding under the Mg^{2+}-induced reactivation conditions. The AlF-inhibited enzyme was incubated in the presence of 10 mM Mg^{2+} with the indicated concentrations of $^{86}Rb^+$ under the same conditions as in Fig. S3*B*, and the amount of bound $^{86}Rb^+$ was determined (blue circles). Data from Fig. 1*A* for the amount of $^{86}Rb^+$-binding in the absence of Mg^{2+} (red circles) was re-plotted for comparison. Data for $^{86}Rb^+$-binding were calculated as a percentage of the maximum value. The percentage of "suppressed" ATPase activities by Rb^+ was also re-plotted (thus opposite dependence as seen in Fig. S3*B*), setting its maximum "suppression" extent to 100%. The apparent affinities of Rb^+ for each measurement are indicated in the figure.

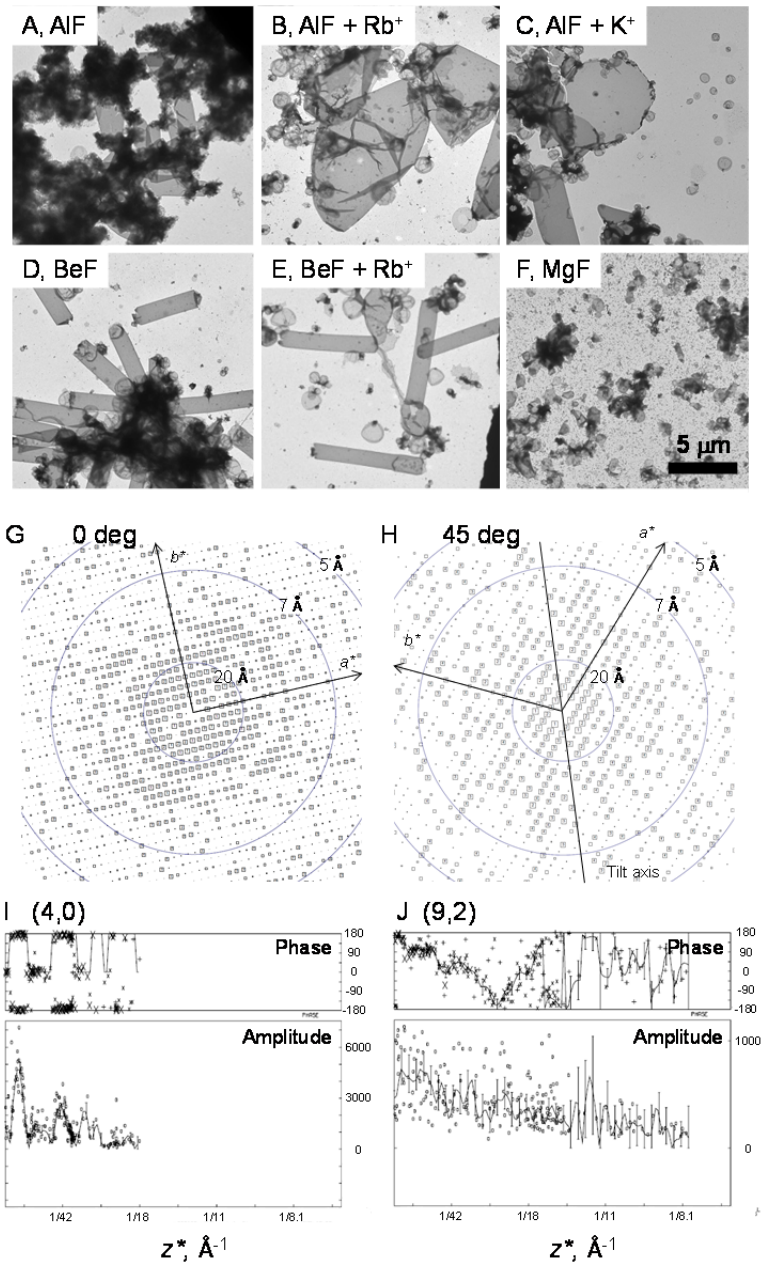

Fig. S6. *Two-dimensional crystals of H^+,K^+-ATPase with phosphate analogues and Rb^+.* (*A*-*F*) Micrographs of negatively-stained 2D crystals grown in the presence of various phosphate analogues in combination with Rb^+ or K^+, as indicated in the figure. All micrographs were obtained at the same magnification (scale bar [5 μm] is shown in panel *F*). (*G*, *H*) IQ plot (34) calculated from a non-tilted (*G*) or 45º tilted (*H*) image of a frozen-hydrated 2D crystal, taken with a liquid helium-cooled cryo-electron microscope. (*I*, *J*) Phases (upper panels) and amplitudes (lower panels) of the representative lattice lines (4,0) (*I*) and (9,2) (*J*) from the 3D data set are shown.

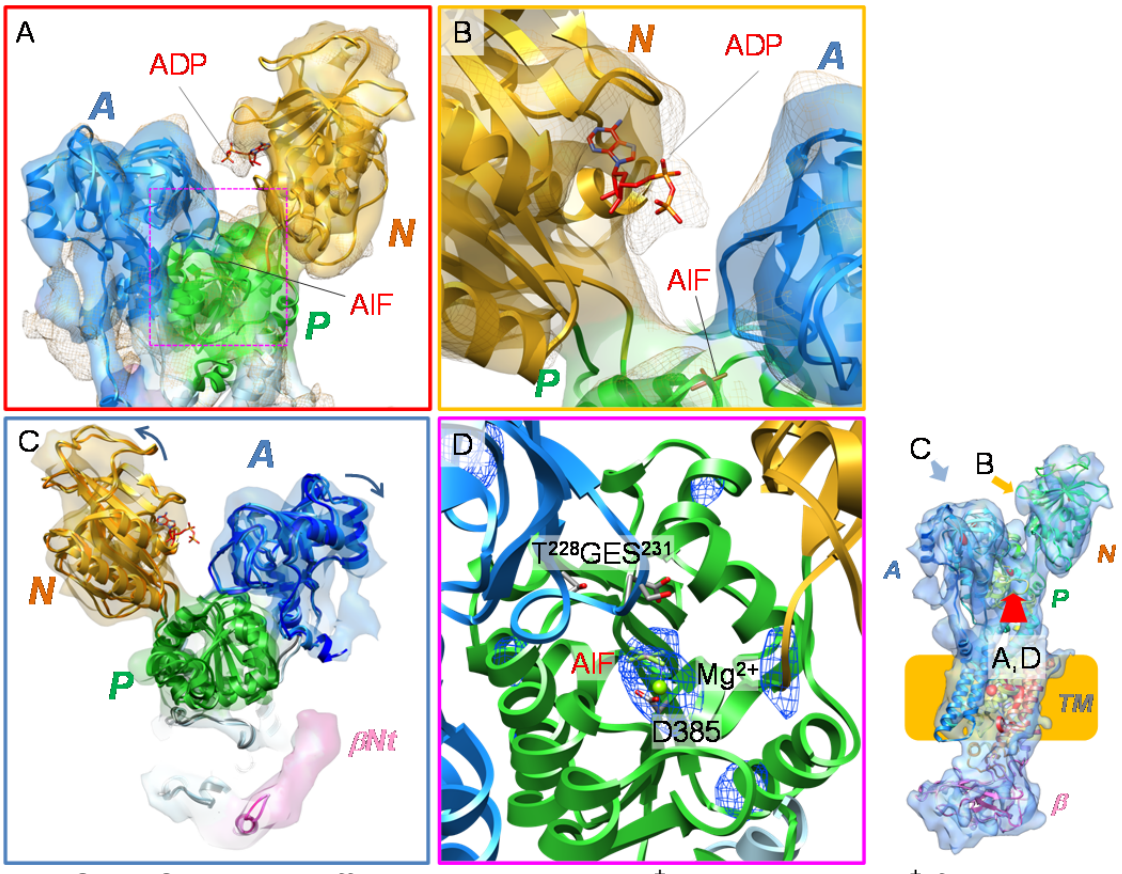

Fig. S7. *Structural difference between (Rb$^+$)E2~AlF and Rb$^+$-free E2AlF at their cytoplasmic domains.* (*A*) Molecular surface (1 σ) represents the EM map of (Rb$^+$)*E2*~AlF with the corresponding homology model with bound AlF (red stick) at the P domain (green) superimposed. The EM map of Rb$^+$-free *E2*AlF is shown as a yellow mesh, and bound ADP (stick) at the N domain (yellow) is indicated. (*B*) Close-up view of the ADP-binding site. (*C*) Comparison of the domain movement induced by Rb$^+$-binding. Homology models of Rb$^+$-free *E2*AlF (ribbon model with dark colors) and (Rb$^+$)*E2*~AlF (light colors) are superimposed into the EM map of (Rb$^+$)*E2*~AlF (surface). Arrows indicate Rb$^+$-induced movement of A and N domains (see also Movie S2). (*D*) Close-up view of the catalytic reaction center of the P domain (indicated by the magenta box in *A*). The invariant D385 and TGES motif are indicated as stick models. Highly contoured density (4 σ) distributed on the AlF-Mg^{2+}-D385 complex is shown in blue mesh. The lower right-hand panel indicates the viewpoints for each panel (*A*-*D*).

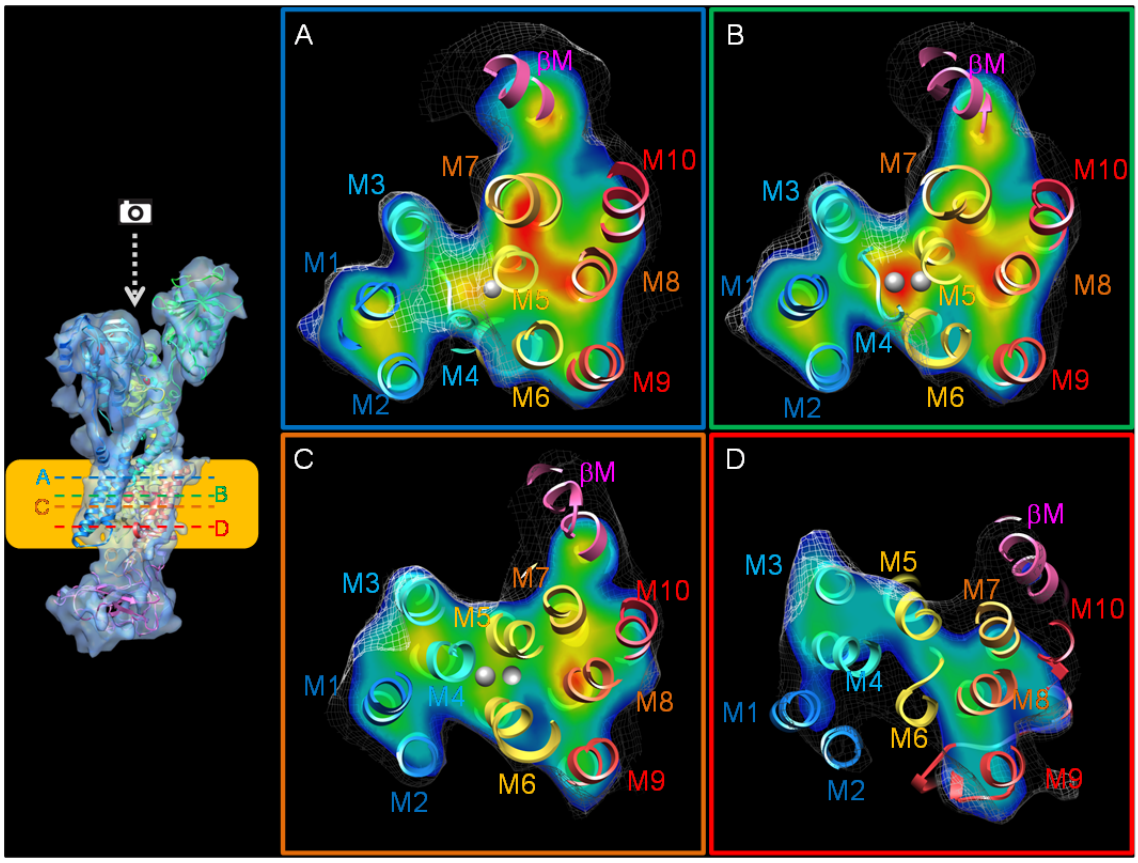

Fig. S8. *Horizontal sections of the TM region viewed from the cytoplasmic side of the membrane.* The positions for each section (*A*-*D*) are indicated as color lines in the whole structure (left). Mesh represents the EM density map (1σ) of (Rb^+)*E2*~AlF, with its homology model superimposed (as in Fig. 2). Cross-sections parallel to the membrane plane show the contour level at the indicated plane (color gradually changes from blue (1σ) to red (5σ) as in Fig. 2).

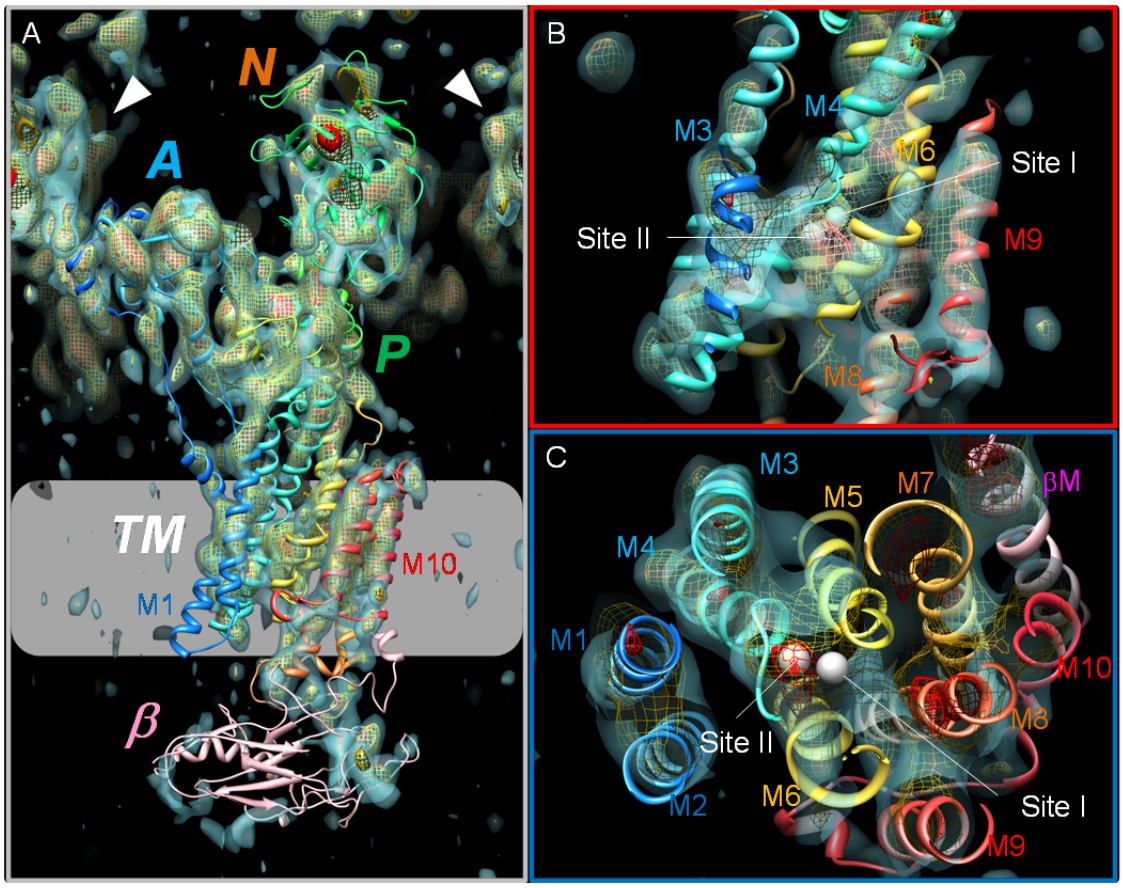

Fig. S9. *Sharpened EM map of (Rb^+)E2~AlF to which a B-factor of -400 was applied.* The molecular surface represents the EM density map contoured to 1.7 σ (light blue), with a superimposed homology model of H^+,K^+-ATPase (ribbon, as in Fig. 2*A*). Highly contoured densities are shown as yellow (2.4 σ) and red (4 σ) mesh, and a superimposed homology model as in Fig. 2. Several important structural components, including cytoplasmic domains and TM helices, are highlighted in the figure. (A) Whole structure viewed from parallel to the membrane normal. White arrowheads indicate a symmetry-related molecule in the 2D crystal. The gray box indicates the approximate location of the membrane. (*B*, *C*) Closed view of the TM region, from a viewpoint parallel to the membrane normal (*B*) or from the cytoplasmic side (*C*). White spheres indicate putative cation binding sites (site I and site II) in our homology model.

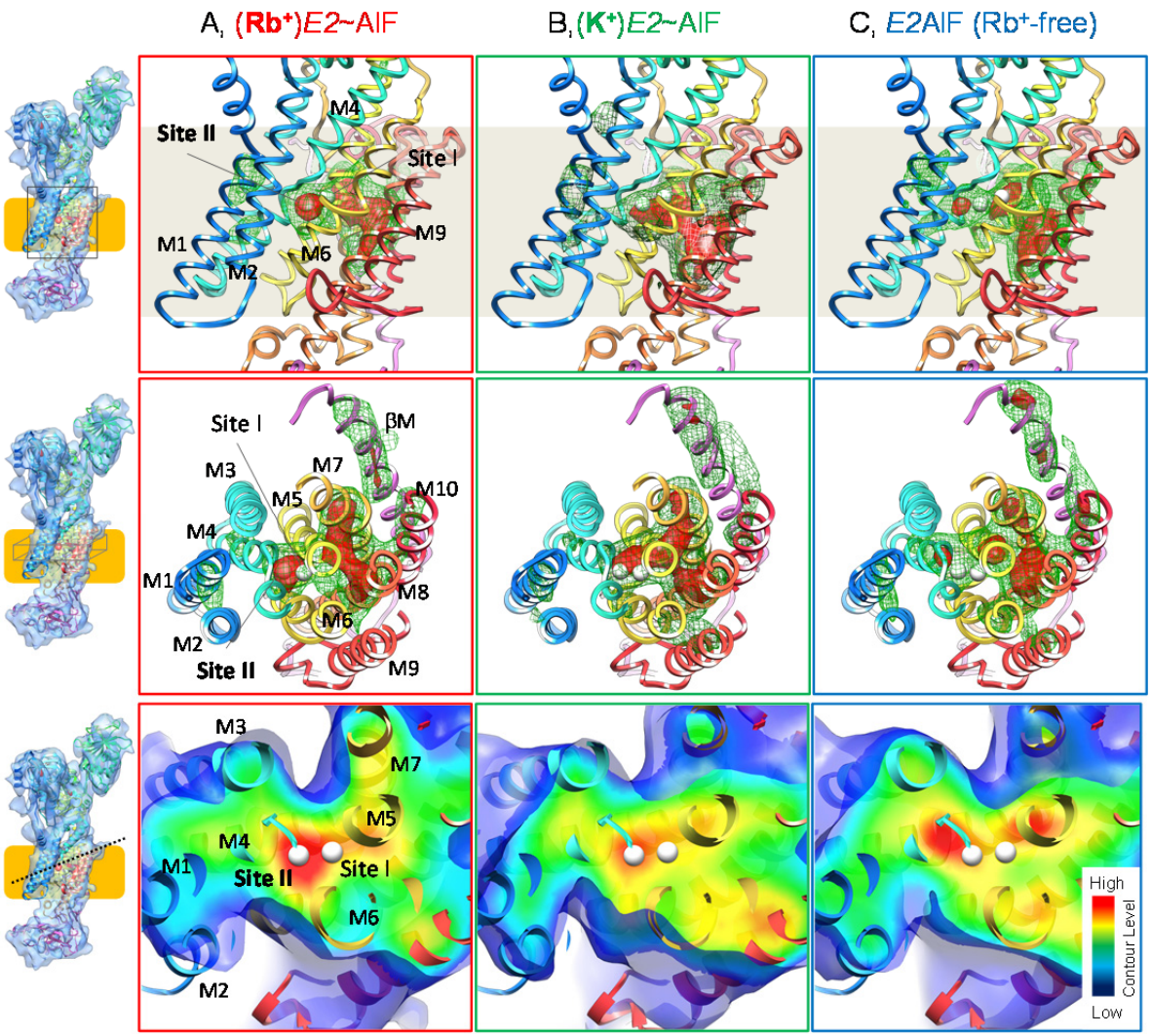

Fig. S10. *EM densities at the cation binding site.* The cation binding sites of (Rb$^+$)*E2*~AlF, (K$^+$)*E2*~AlF, Rb$^+$-free *E2*AlF (*A*, *B*, and *C*, respectively), viewed parallel to the membrane normal (upper panels), or approximately perpendicular to the membrane from the cytoplasmic side (middle panels). Green mesh and red surface represent EM densities with 4 or 5 σ contour levels for (Rb$^+$)*E2*~AlF, and the corresponding contour levels of other structures, respectively (see Methods, and Fig. S14 for details). Cross-sections of the cation-binding sites of the indicated conformations, viewed from the cytoplasmic side (the position is indicated by the dotted line at the left) are shown (lower panels). Surface color displays the contour level at the indicated plane, the color of which gradually changes from blue (low) to red (high). Color codes for the homology models are the same as in Fig. 2*A*.

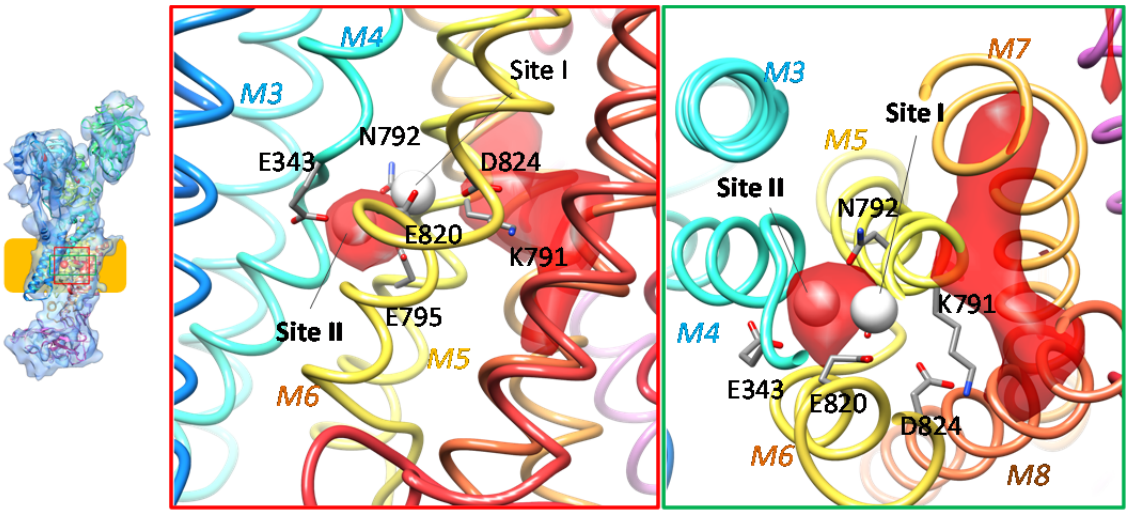

Fig. S11. *Cation-binding site of the (Rb^+)E2~AlF homology model.* A homology model (ribbon) of the putative cation-binding pocket of H^+,K^+-ATPase, with the EM density map contoured to 5 σ (red surface). Selected residues in M4, M5, and M6 of the H^+,K^+-ATPase involved in cation coordination are represented as sticks. White spheres indicate the position of bound K^+ in the Na^+,K^+-ATPase structure.

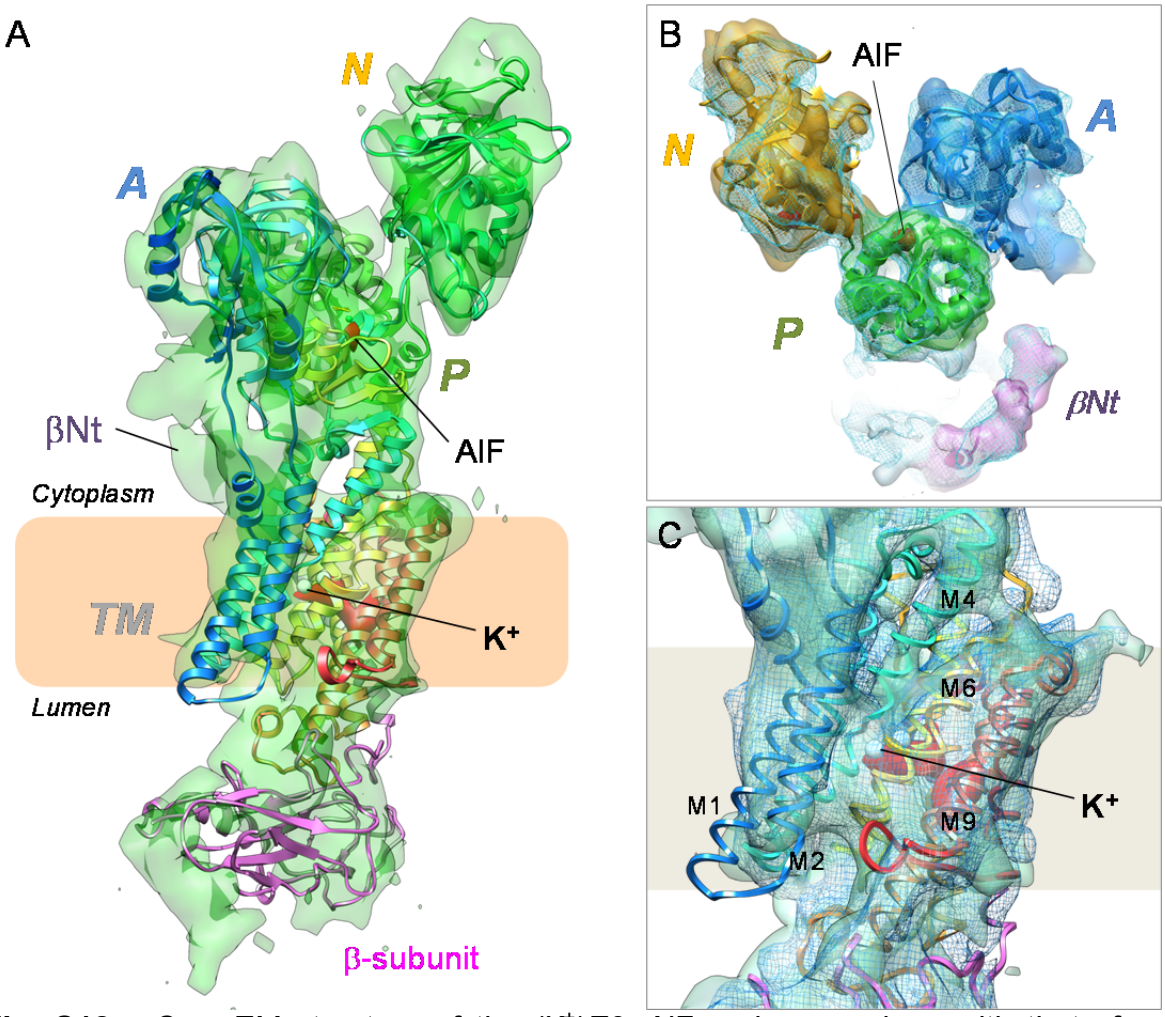

Fig. S12. *Cryo-EM structure of the (K^+)E2~AlF and comparison with that of (Rb^+)E2~AlF.* (*A*)The molecular surface represents the EM density map contoured to 1 σ (light green), with a superimposed homology model of H^+,K^+-ATPase (ribbon, as in Fig. 2*A*). Highly contoured densities are shown as a red surface. Several important structural components, including bound Rb^+, are highlighted in the figure. (*B*, *C*) Comparison of the cytoplasmic domains (*B*) and TM domain (*C*) of the K^+-bound (surface) and Rb^+-bound (mesh) structures.

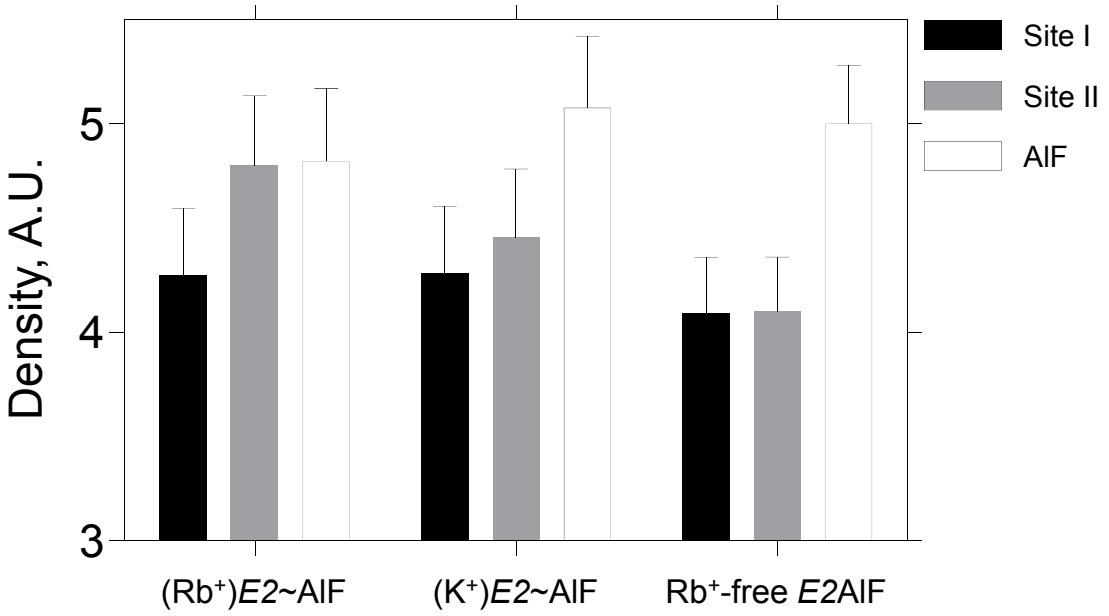

Fig. S13. *Bootstrap resampling analysis.* Mean values and their standard deviations (error bars) of the EM density at site I (closed bars), site II (grey bars), and the AlF-Mg^{2+}-Asp385 complex at the P domain (open bars, AlF) in each EM map were estimated by bootstrap resampling analysis (see also Methods). The plotted values are scaled as described in Fig. S15. Similar contour levels found at the AlF provide a cross-validation for proper comparison of the EM density at the cation binding sites.

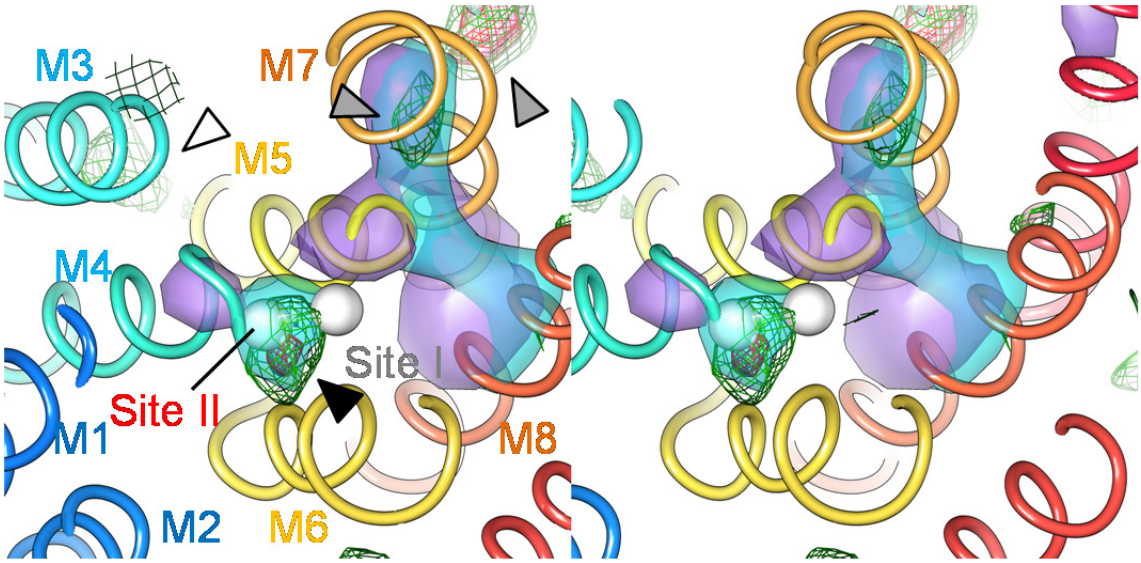

Fig. S14. *Stereo view of the real-space subtraction.* EM density maps resulting from the difference between two structures [(Rb^+)*E2*~AlF] – [Rb^+-free *E2*AlF] in real space are shown as green (1 σ) and red (1.4 σ) mesh. The cyan and purple surface represents the 5 σ-contoured EM map of (Rb^+)*E2*~AlF and Rb^+-free *E2*AlF, respectively, and the ribbon represents a homology model of (Rb^+)*E2*~AlF. Black arrowheads indicate the subtracted density which most likely represents bound Rb^+. Other densities found within the relatively highly-contoured (more than 2 σ) volume of the (Rb^+)*E2*~AlF TM domain (grey arrowheads) can only be observed at M7 and βM. These densities might be due to a subtle difference in their conformation and/or stability between the two maps. Other similar contours are mostly observed outside or at the outermost edge of the 1 σ-contoured molecular envelope (*e.g.,* white arrowhead near M3). It is notable that the asymmetric distribution of the subtracted density near site II (black arrowhead) is likely to be affected by the strong density of Rb^+-free *E2*AlF found at the central axis of the M4 helix. The panel shows a section of the TM domain, viewed from the cytoplasmic side of the membrane.

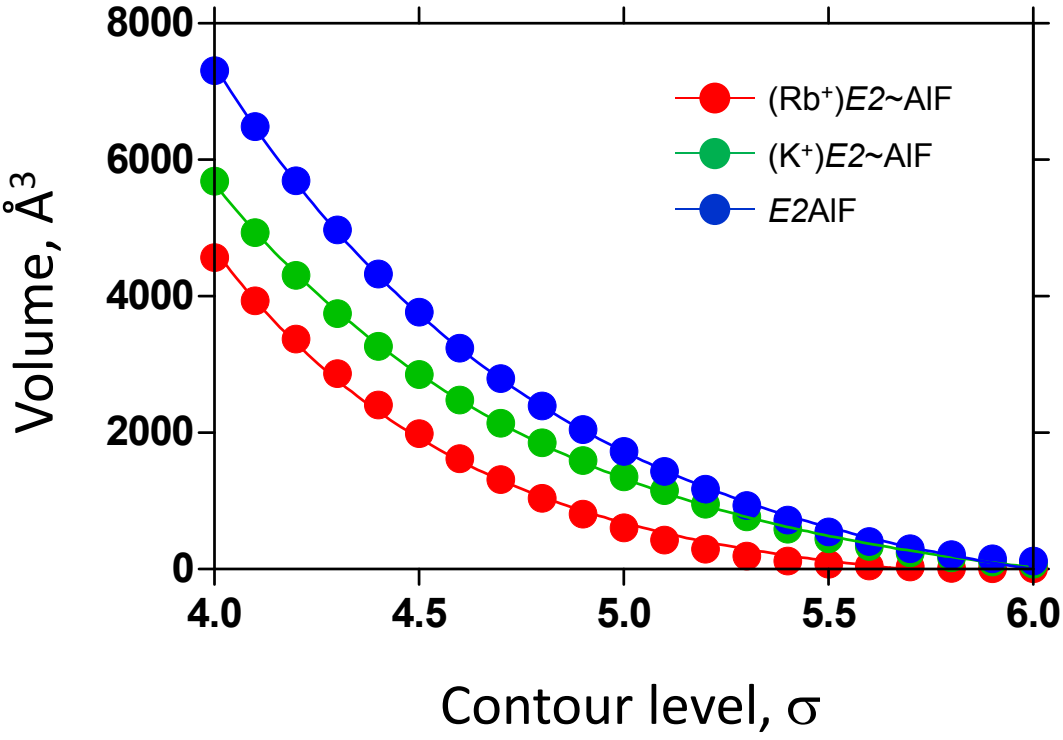

Fig. S15. *Trends in the highly contoured densities of the EM structures.* Observed volumes (Å^3) of the EM density maps against the contour level (in σ) for the (Rb$^+$)*E2*~AlF (red), (K$^+$)*E2*~AlF (green), and Rb$^+$-free *E2*AlF (blue) are plotted. For proper comparison of the strong density at the cation-binding sites in each EM map, the contour levels for (K$^+$)*E2*~AlF and Rb$^+$-free *E2*AlF displayed in Fig. 2 and Fig. S10 were adjusted to that of (Rb$^+$)*E2*~AlF, depending on the volume. See Methods for details.

Movie S1. *Cryo-EM structure of H^+,K^+-ATPase in (Rb^+)E2~AlF state.* Molecular surface shows the EM map of (Rb^+)*E2*~AlF at 1 σ (A domain, blue; P domain, green; N domain, Orange; TM, light blue; β-subunit, pink) and 5 σ (red), with superimposed homology model (colour for TM helices (M1-M10) gradually changes from blue to red).

Movie S2. *Rb^+-induced rearrangement of the cytoplasmic domains.* Sequential appearance of *E2*~AlF (dark colours) and (Rb^+)*E2*~AlF (light colours) shows Rb^+-induced movement of A and N domains relative to the P domain. Structures were viewed from the same direction as in Fig. 7*C*.

Movie S3. *Horizontal sections throughout the TM region of (Rb^+)E2~AlF.* Cross-sections of the TM region (as shown in Fig. S8) are sequentially displayed. Positions are indicated in the upper left. Color codes are as in Fig. S8.

Table S1. *Electron crystallographic data*

Two-dimensional crystal		
Space group	$p22_12_1$	
Lattice constants	a = 141.0 Å, b = 110.6 Å,	
	c = 320.0 Å (assumed), γ = 90.0°	
Electron micrographs	No. of image	
Approximate tilt angle	(Rb^+)*E2*~AlF	(K^+)*E2*~AlF
0°	4	6
20°	23	58
45°	139	94
60°	82	120
Total	248	278
Resolution limit	(Rb^+)*E2*~AlF	(K^+)*E2*~AlF
For map		
Parallel to the membrane plane	8.0 Å	8.0 Å
Perpendicular to the membrane plane	9.2 Å	9.4 Å
For merging		
Parallel to the membrane plane	7.0 Å	8.0 Å
Perpendicular to the membrane plane	8.2 Å	9.4 Å
Maximum tilt angle	63.7°	62.6°
Range of underfocus	8300-34800 Å	6700-38800 Å
Number of observed reflections	39197	42014
Unique reflections	5601	4122
IQ-weighted phase residual[a]	35.6° (Overall)	36.9° (Overall)
	26.2 (-15.6 Å)	25.4 (-17.9 Å)
	37.2 (15.6-11.1 Å)	39.4 (17.9-12.6 Å)
	49.0 (11.1-9.0 Å)	46.7 (12.6-10.3 Å)
	54.9 (9.0-7.8 Å)	54.2 (10.3-8.9 Å)
	53.2 (7.8-7.0 Å)	57.7 (8.9-8.0 Å)
Overall IQ-weighted R-factor	0.38	0.42

[a] 90° is random. Used reflections are less than IQ 6.

SI References

1. Abe K, Tani K, Fujiyoshi Y (2010) Structural and functional characterization of H^+,K^+-ATPase with bound fluorinated phosphate analogs. J Struct Biol 170:60-68.
2. Montes MR, et al. (2011) Rb^+ occlusion stabilized by vanadate in gastric H^+/K^+-ATPase at 25 °C. Biochim Biophys Acta 1808:316-322.
3. Wallmark B et al. (1987) Inhibition of gastric H^+,K^+-ATPase and acid secretion by SCH28080, a substituted pyridyl(1,2a)imidazole. *J Biol Chem* 262:2077-2084.
4. González-Lebrero RM et al. (2002) The occlusion of Rb^+ in the Na^+/K^+-ATPase. I. The identity of occluded states formed by the physiological or the direct routes. Occlusion/deocclusion kinetics through the direct route, *J Biol Chem* 277:5910–5921.
5. Abe K, Tani K, Nishizawa T, Fujiyoshi Y (2009) Inter-subunit interaction of gastric H^+,K^+-ATPase prevents reverse reaction of the transport cycle. EMBO J 28:1637-1643.
6. Jensen A-ML, Sørensen T L-M, Olesen C, Møller JV, Nissen P (2006) Modulatory and catalytic modes of ATP binding by the calcium pump. EMBO J 25:2305-2314.
7. Olesen C et al. (2007) The structural basis of calcium transport by the calcium pump. Nature 450:1036-1042.
8. Toyoshima C, Norimatsu Y, Iwasawa S, Tsuda T, Ogawa H (2007) How processing of aspartylphosphate is coupled to luminal gating of the ion pathway in the calcium pump. Proc Natl Acad Sci USA 104:19831-19836.
9. Post RL, Kume S (1973) Evidence for an aspartyl phosphate residue at the active site of sodium and potassium ion transport adenosine triphosphatase. *J Biol Chem* 248:6993-7000.